



HAL
open science

Yttrium speciation in sulfate-rich hydrothermal ore-forming fluids

Qiushi Guan, Yuan Mei, Barbara Etschmann, Marion Louvel, Denis Testemale, Evgeniy Bastrakov, Joël Brugger

► **To cite this version:**

Qiushi Guan, Yuan Mei, Barbara Etschmann, Marion Louvel, Denis Testemale, et al.. Yttrium speciation in sulfate-rich hydrothermal ore-forming fluids. *Geochimica et Cosmochimica Acta*, 2022, 325, pp.278-295. 10.1016/j.gca.2022.03.011 . hal-03810407

HAL Id: hal-03810407

<https://hal.science/hal-03810407>

Submitted on 11 Oct 2022

HAL is a multi-disciplinary open access archive for the deposit and dissemination of scientific research documents, whether they are published or not. The documents may come from teaching and research institutions in France or abroad, or from public or private research centers.

L'archive ouverte pluridisciplinaire **HAL**, est destinée au dépôt et à la diffusion de documents scientifiques de niveau recherche, publiés ou non, émanant des établissements d'enseignement et de recherche français ou étrangers, des laboratoires publics ou privés.

Yttrium speciation in sulfate-rich hydrothermal ore-forming fluids

Qiushi Guan^{1,2}, Yuan Mei^{2,*}, Barbara Etschmann¹, Marion Louvel³, Denis Testemale⁴,
Evgeniy Bastrakov⁵, and Joël Brugger^{1,*}

1. School of Earth, Atmosphere and the Environment, Monash University, Clayton, VIC 3800, Australia

2. CSIRO Mineral Resources, Kensington WA 6151, Australia

3. Institute for Mineralogy, WWU Muenster, D-48149 Germany

4. CNRS, Université Grenoble Alpes, Institut NEEL, F-38000 Grenoble, France

5. Geoscience Australia, GPO Box 378, Canberra, ACT, 2601, Australia

*Corresponding authors:

Yuan Mei (Yuan.Mei@csiro.au);

Joël Brugger (joel.brugger@monash.edu)

Abstract

Rare Earth elements (REE) are gaining importance due to their increasing industrial applications and usefulness as petrogenetic indicators. REE-sulfate complexes are some of the most stable REE aqueous species in hydrothermal fluids, and may be responsible for REE transport and deposition in a wide variety of geological environments, ranging from sedimentary basins to magmatic hydrothermal settings. However, the thermodynamic properties of most REE-sulfate complexes are derived from extrapolation of ambient temperature data, since direct information on REE-sulfate complexing under hydrothermal conditions is only available for Nd, Sm and Er to 250 °C (Migdisov and William-Jones, 2008, 2016).

We employed *ab initio* molecular dynamics (MD) simulations to calculate the speciation and thermodynamic properties of yttrium(III) in sulfate and sulfate-chloride solutions at temperatures and pressures up to 500 °C and 800 bar. The MD results were complemented by *in situ* X-ray absorption spectroscopy (XAS) measurements. Both MD and XAS show that

30 yttrium(III) sulfate complexes form and become increasingly stable with temperature
31 (≥ 200 °C). The MD results also suggest that mixed yttrium-sulfate-chloride complexes (that
32 cannot be distinguished from mixtures of chloride and sulfate complexes in XAS experiments)
33 form at ≥ 350 °C. Two structures with two different Y(III)-S distances (monodentate and
34 bidentate) are observed for Y(III)-sulfate bonding. The formation constants, derived via
35 thermodynamic integration, for the Y(III) mono- and di-sulfate complexes parallel the trends
36 for those of Nd, Sm and Er determined experimentally to 250 °C.

37 The derived formation constants were used to fit revised Helgeson-Kirkham-Flowers
38 equation-of-state parameters that enabled calculation of formation constants for $\text{Y}(\text{SO}_4)^+$ and
39 $\text{Y}(\text{SO}_4)_2^-$ over a wide range of temperatures and pressures. The presence of sulfate increases
40 the solubility of Y(III) under specific conditions. Since the stability of sulfate is redox sensitive,
41 Y(III) solubility becomes highly redox-sensitive, with rapid precipitation of Y minerals upon
42 destabilisation of aqueous sulfate.

43 Keywords: yttrium, rare earth elements, sulfate, *ab initio* molecular dynamics,
44 thermodynamics, *in situ* XAS.

45

46 1 Introduction

47 Rare earth elements (REE) are the 15 metals from lanthanum to lutetium; yttrium and
48 scandium are often added, due to similar geochemical behaviour. These metals are in
49 increasing demand due to their unique applications (Naumov, 2008; McLemore, 2011; Massari
50 and Ruberti, 2013); their supply is highly concentrated in a few countries, resulting in their
51 classification as critical minerals (Ram et al., 2019; Jowitt et al. 2020). Hydrothermal processes
52 play an important role in the enrichment of REE (Migdisov et al., 2016), either in conjunction
53 with magmatic processes (e.g. the world's largest REE deposit at Bayan Obo, China; Smith et

54 al., 2000) or in purely hydrothermal settings over a wide range in conditions (e.g., the Iron
55 Oxide Copper Gold (IOCG) deposit at Olympic Dam, South Australia; [Bastrakov et al., 2007](#);
56 [Xing et al. 2019](#); or the low temperature (<125 °C), basinal-brine related deposits of the Browns
57 Ranges, Northern Australia; [Richter et al., 2018](#); [Nazari-Dehkordi et al., 2020](#)). The near
58 universal occurrence of the REE at low, but detectable levels, together with slight, systematic
59 differences in their responses to changing physico-chemical conditions, make them powerful
60 petrologic indicators for a wide variety of geological environments ([Brugger et al., 2008](#);
61 [Williams-Jones et al., 2012](#); [Migdisov et al. 2016](#)).

62 In order to develop more effective exploration methods for REE deposits and to optimise
63 the applications of REE as petrogenetic tools, it is beneficial to understand the mechanism of
64 REE transport in hydrothermal fluids. REE transport is a function of solution composition
65 (transporting and precipitating ligands, including Cl⁻, F⁻, SO₄²⁻, PO₄³⁻, CO₃²⁻, etc...), other
66 chemical parameters such as pH, temperature (T) and pressure (P), and the stability of REE-
67 bearing minerals. As a ligand, sulfate is known to play a critical role in many geological
68 environments, including seafloor vent fluids ([Bach et al., 2003](#); [Wang et al., 2020](#)); volcano-
69 hydrothermal systems ([Inguaggiato et al., 2015](#)); subduction fluids ([Debret and Sverjensky,](#)
70 [2017](#); [Rielli et al., 2017](#)); and many magmatic hydrothermal systems ([Panina, 2005](#)). REE form
71 strong sulfate complexes under ambient conditions ([Gimeno Serrano et al., 2000](#); [Lozano et al.](#)
72 [2020](#)) and a direct link between sulfate-rich fluids and REE mineralization has been reported
73 in a variety of deposits. Sulfate is for instance abundant in fluid inclusions associated with REE
74 mineralisation in the granite-related Capitan Pluton, New Mexico ([Banks et al., 1994](#); up to
75 24,210 ppm SO₄²⁻) and in the quartz syenite-hosted bastnaesite deposits of the Gallinas
76 Mountains, New Mexico ([Williams-Jones et al., 2000](#); [McLemore, 2011](#)). Though most REE
77 deposits are associated with magmatic carbonatites ([González-Álvarez et al., 2021](#)), late-
78 magmatic mobilisation by hydrothermal fluids played an important role in upgrading the ores,

79 and sulfate-rich fluids are associated with many of these deposits, including the Mianning-
80 Dechang REE belt, western Sichuan province, China (Xie et al., 2015), and the Huanglongpu
81 carbonatites, China (Cangelosi et al., 2020).

82 Based on these observations, Cui et al. (2020) and Cangelosi et al. (2020) recently
83 suggested that REE-sulfate complexes, rather than REE chloride complexes, may account for
84 REE transport in these environments, despite the higher availability of chloride in crustal fluids
85 (Migdisov and Williams-Jones, 2014). However, data on the speciation and thermodynamic
86 properties of most REE-sulfate complexes are limited to extrapolations from room temperature
87 (Wood, 1990; Haas et al., 1995; Migdisov et al., 2016) and a few experimental studies to 250°C
88 (Migdisov et al., 2006; Migdisov and William-Jones 2008). Room-temperature
89 thermodynamic data for aqueous REE complexes, including $Y(SO_4)^+$ and $Y(SO_4)_2^-$, were
90 selected by Spahiu and Kastriot (1995) based on an extensive literature review. Schijf and
91 Byrne (2004) determined the formation constants of $REE(SO_4)^+$ at ambient conditions (ionic
92 strength = 0.66 m and $T = 25^\circ C$) by solubility experiments, showing a relatively higher
93 stability for LREE compared to HREE. Migdisov and Williams-Jones (2008) (including a re-
94 interpretation of the Nd data published by Migdisov et al., 2006) measured the temperature
95 dependence of the formation constants of Nd(III)-, Sm(III)- and Er(III) mono- and di-sulfate
96 complexes by spectrophotometry, finding that the di-sulfate complex increases in stability
97 relative to the mono-sulfate complex as temperature increases from 25°C to 250°C, the
98 maximum experimental temperature. In addition to these experimental studies, theoretical
99 quantum-chemical studies have characterised the stoichiometry and geometry of Y(III)-aqua,
100 -chloride and -fluoride complexes under ambient, hydrothermal and subduction conditions.
101 Ikeda et al. (2005a,b) characterised the hydration structure of Y^{3+} at room temperature, and Liu
102 et al. (2012) calculated the pK_a of the hydrolysis reactions of Y^{3+} at room temperature. Guan
103 et al. (2020) combined *ab initio* molecular dynamic method and *in situ* X-ray absorption

104 spectroscopy to determine the Y(III)-Cl complexes present at temperature up to 500 °C and
105 their formation constants, and [Stefanski and Jahn \(2020\)](#) used *ab initio* molecular dynamics to
106 characterise the geometry and thermodynamics of Y(III)-Cl and Y(III)-F complexes under
107 subduction zone conditions (800 °C, 13 and 45 kbar). To date, no quantum chemical study of
108 Y(III)-sulfate (or any other REE-sulfate) complexes are reported, and experiments are limited
109 to temperatures of 250 °C. Recently, [Zhang and Yan \(2022\)](#) used classical MD simulations to
110 show that heavy REE (Lu) form more stable aqueous complexes than light REE (La) with a
111 number of ligands, including sulfate; however, the classical MD method used in their study
112 provides relatively large discrepancy between MD-derived and experimental stability constants
113 (3-4 log units for sulfate).

114 Here, we aim to improve our understanding of the role of sulfate complexes in the mobility
115 of yttrium using a combination of *ab initio* molecular dynamics (MD) simulations and *in situ*
116 X-Ray Absorption Spectroscopy (XAS) to decipher the nature and geometry of yttrium(III)-
117 sulfate complexes to magmatic-hydrothermal conditions. Thermodynamic properties for key
118 species are then estimated using thermodynamic integration. This combined approach can
119 provide accurate information about the geometry and stability of metal complexes in
120 hydrothermal fluids ([Mei et al., 2013, 2014, 2015a, 2015b, 2016; Brugger et al., 2016;](#)
121 [Etschmann et al., 2019](#)). Based on the new results, we discuss the mobility of Y(III) in both
122 sulfate-rich and sulfate-chloride solutions under hydrothermal conditions, and provide a better
123 understanding of REE transport and mineral precipitation in hydrothermal systems.

124

125 2 Method

126 2.1 *Ab initio* molecular dynamics

127 The *ab initio* molecular dynamics simulations were conducted with the
128 CP2K/QUICKSTEP (Kühne et al., 2020) and Car-Parrinello Molecular Dynamics (CPMD,
129 version 3.1.17, Car and Parrinello, 1985) packages. Both CP2K and CPMD were used for
130 unconstrained simulations to study the geometry of Y-sulfate complexes, while CPMD was
131 used for the thermodynamic integration simulations aimed at retrieving formation constants for
132 the most important complexes. Due to differences in methods (Car-Parrinello vs. Born-
133 Oppenheimer), *ab initio* MD simulations by CPMD are more CPU intensive than with CP2K.
134 For example, one picosecond (ps) of data required ~1,400 CPU hours using CPMD for a
135 simulation box containing 55 water molecules with a density of 1.03 g/cm³ (300 °C, box 3,
136 Table 1), but one order of magnitude more resources (~14,400 CPU hour per ps) are required
137 for a simulation box containing twice the amounts of water molecules (box 1, Table 1). In
138 contrast, 460 CPU hours were required to collect 1 ps of real time data using CP2K for a
139 simulation box with 111 water and a density of 1.11 g/cm³ (200 °C, box 2, Table 1). In this
140 study, we first compared the unconstrained MD results (e.g., bond distance) between CP2K
141 and CPMD, finding no significant difference in the predictions from both codes (details in the
142 Results section below); we employ the more efficient CP2K for longer (>40 ps) MD
143 simulations, but we use the framework we developed in previous studies with CPMD for the
144 derivation of stability constants for ligand exchange reactions using thermodynamic integration.

145 CP2K and CPMD employ the Kohn-Sham (Kohn and Sham, 1965) density functional
146 theory with mixed Gaussian and Slater plane wave basis sets, respectively. The temperature
147 was controlled by a Nosé-Hoover chain thermostat; periodic boundary conditions were applied
148 to eliminate surface effects; and all simulations were conducted in the NVT canonical ensemble.
149 In CP2K, the core electrons were modelled by Goedecker-Teter-Hutter (GTH)

150 pseudopotentials (Goedecker et al., 1996; Hartwigsen et al., 1998; Krack, 2005) and double-
151 zeta valence polarized (DZVP) basis sets (VandeVondele and Hutter 2007) together with the
152 BLYP exchange correlation functional (Becke, 1988; Lee et al., 1988). In CPMD, the BLYP
153 exchange correlation functional was also used but in combination with the most-commonly
154 used Troullier-Martins norm-conserving pseudopotentials (Troullier and Martins, 1991).
155 Previous studies (e.g., Lin et al., 2012; Mei et al., 2015a) have shown that the BLYP functional
156 can accurately describe aqueous metal-ligand interactions, especially at high temperature. In
157 CP2K, a timestep 0.5 femtosecond (fs) was chosen, but a shorter simulation timestep of
158 0.073 fs was required in CPMD. The shorter time step required by the Car-Parrinello MD in
159 CPMD is responsible for most of the increase in processing resources relative to CP2K.

160 Simulations were conducted at 200-500 °C, 800 bar to compare with XAS experiments.
161 Sulfate and chloride concentrations of 1-2 molal (*m*) were chosen to represent the hydrothermal
162 fluids with manageable computing time, at ionic strengths that are common in geological fluids
163 and manageable using commonly used activity coefficient models (Brugger et al. 2016;
164 Helgeson et al., 1981). The densities of the solutions were set according to the equation of state
165 of NaCl(aq) at targeted P-T conditions (Driesner, 2007; Driesner and Heinrich, 2007). Radial
166 distribution functions (RDF) and coordination numbers (integrals of RDF) were calculated
167 using VMD (Humphrey et al., 1996). Details of the simulation boxes and software used are
168 listed in Table 1.

169

170 2.2 *Ab initio* thermodynamic integrations

171 *Ab initio* MD provides information on the geometric and stoichiometric properties of Y-
172 sulfate complexes; however, in most cases the ligand exchange rates are longer than the time
173 scale of the *ab initio* MD simulations achievable with current high performance computing
174 infrastructure (typically <<100 picoseconds (ps); Mei et al., 2015a, Guan et al., 2020). Even

175 though ligand residence times decrease with increasing temperature to a point where individual
176 ligand exchange reactions can be easily observed via *ab initio* MD, the exchange rates are
177 generally not sufficient to allow measurements of the relative stabilities of the various
178 complexes by examining the distribution of species in the simulations. In the case of REE at
179 room temperature, the water and sulfate residence times vary in the range 100-1000 ps (Fay et
180 al., 1969; Richens 2005). Different methods have been developed to provide accurate statistical
181 sampling with achievable computing resources. Here we use the thermodynamic integration
182 method (Sprik, 1998; Sprik & Ciccotti, 1996) to determine the equilibrium constants of ligand
183 exchange reactions. As previous studies introduced and benchmarked this method for metals
184 complexed to small inorganic ligands in hydrothermal conditions (e.g., Mei et al., 2013), only
185 a brief summary is provided here. A predefined reaction path was set by defining the distance
186 (r) between the metal (Y) and the ligand (SO_4^{2-}) from the equilibrium distance (r_I) to a distance
187 (r_{II}) where there are no interactions between Y(III) and SO_4^{2-} . This is achieved by constraining
188 the Y-S distance. The average force ($f(r)$) required to constrain the Y(III)-S(SO_4^{2-}) distance at
189 each step can be calculated from simulations conducted for at least 7 ps, which is sufficient
190 time to sample a significant representation of Y(III) configurations. The free energy surface of
191 the ligand exchange reaction was obtained by integrating $f(r)$ over the constrained distance r :

$$192 \quad \Delta A_{I \rightarrow II} = - \int_{r_I}^{r_{II}} f(r) dr \quad (1)$$

193 The free energy difference of the reaction is independent from the reaction path (Guan et
194 al., 2020). The Gibbs free energy of the reaction, $\Delta_r G$, is approximated as $\Delta A_{I \rightarrow II}$ by assuming
195 that the pressure is constant during the reaction (Mei et al., 2013). The constrained MD
196 simulations were run under all the conditions of box 3 (Table 1) with CPMD. To further test
197 the effect of the box size on the results of the thermodynamic integrations, one set of
198 thermodynamic integration calculations was conducted within simulation box containing 111
199 water molecules at 300 °C (box 1). Because of the high demand for CPU resources of the

200 simulation in such a big box, we reduced the minimum simulation time to ~5 ps (instead of
201 7 ps) at each distance in this calculation.

202 The standard state Gibbs free energy of reaction ($\Delta_r G^\ominus$) can be derived from the measured
203 Gibbs free energy of reaction ($\Delta_r G$) using:

$$204 \quad \Delta_r G^\ominus = \Delta_r G + RT \ln \frac{c_{AY_A} \cdot c_{BY_B}}{c_c \gamma_c \cdot c_{DY_D}} \quad (2)$$

205 where c_i is the concentration of the i^{th} compound in the reaction $A + B \rightarrow C + D$, and γ_i is
206 the activity coefficient of each species; $\Delta_r G^{\ominus,c}$ is calculated assuming $\gamma_i = 1$, and $\Delta_r G^\ominus$ using
207 activity coefficients described in the following paragraph. The concentrations c_i were defined
208 using the initial (at distance r_{I} ; reactants) and final (r_{II} ; products) configurations in the *ab initio*
209 thermodynamic integration. For example, for the reaction $Y^{3+} + SO_4^{2-} = Y(SO_4)^+$, the initial
210 equilibrated simulation box contains 1 m $Y^{3+} + 2$ m SO_4^{2-} ; the final contains 1 m $Y(SO_4)^+ +$
211 1 SO_4^{2-} . For the reaction $Y(SO_4)^+(b) + SO_4^{2-} = Y(SO_4)_2^-$, the concentrations of all species are
212 equal to 1; hence, in this case, no correction is required if activity coefficients are neglected
213 (equation (2)).

214 A more accurate estimate of the standard Gibbs free energy for the complex-forming
215 reactions was obtained using the B-dot extension of the Debye-Hückel theory (Helgeson et al.,
216 1981) to estimate the activity coefficients of the ions in the reaction:

$$217 \quad \log \gamma_i = -\frac{z_i^2 A_\gamma I^{1/2}}{1 + a_i B_\gamma I^{1/2}} + \dot{B}_\gamma I \quad (3)$$

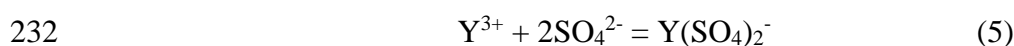
218 where; z_i is the charge of ion i ; I is the ionic strength in molality; a_i is the ion size parameter
219 (\AA); A_γ and B_γ are defined in Tables 1 and 2 in Helgeson and Kirkham (1974), \dot{B}_γ is an
220 empirical parameter taken from Oelkers and Helgeson (1990). This formalism is chosen
221 because of consistency with the Helgeson-Kirkham-Flowers (HKF) (Helgeson et al., 1981;
222 Sverjensky, 1997) equation-of-state (EOS), which is *de facto* the most widely used EOS in
223 hydrothermal geochemistry (e.g., Miron et al. 2019).

224 Formation constants (K) are calculated from:

$$225 \quad \Delta_r G^\ominus = -RT \ln K \quad (4)$$

226 where R is the gas constant and T is the absolute temperature.

227 The errors of the $\Delta_r G$ were estimated using the method proposed by [Allen and Tildesley](#)
228 [\(1987, section 6.4\)](#), which takes into account both systematic and statistical errors. This method
229 was successfully employed in measuring the uncertainties of thermodynamic integration by
230 [Rodinger et al. \(2005\)](#), [Mei et al. \(2018, 2020\)](#) and [Guan et al. \(2020\)](#). The cumulative
231 formation constants ($\log\beta$) for the reaction



233 were calculated by adding the $\log K(P,T)$ for the $\text{Y}^{3+} + \text{SO}_4^{2-} = \text{Y}(\text{SO}_4)^+$ and $\text{Y}(\text{SO}_4)^+ + \text{SO}_4^{2-}$
234 $= \text{Y}(\text{SO}_4)_2^-$ reactions, applying standard error propagation rules.

235 2.3 X-ray absorption spectroscopy (XAS)

236 2.3.1 Sample solutions and XAS measurements

237 MilliQ water and analytical grade yttrium sulfate ($\text{Y}_2(\text{SO}_4)_3 \cdot 8\text{H}_2\text{O}$), Na_2SO_4 , 96% H_2SO_4 ,
238 and NaCl were used to prepare the experimental solutions for XAS measurements ([Table 2](#)).
239 All solutions were prepared gravimetrically.

240 The speciation of yttrium in sulfate and mixed sulfate-chloride solutions was characterised
241 via *in situ* XAS measurements using the high temperature-high pressure cell developed at the
242 Institut Néel/ESRF ([Testemale et al., 2005](#)); the details of the experimental setup are described
243 in [Guan et al. \(2020\)](#). The temperature of the fluid at the beam location was calibrated (e.g.,
244 [Tooth et al., 2013](#); [Louvel et al., 2017](#)) by calculating the density of pure water from
245 measurements of the absorbance and X-ray mass attenuation coefficients tabulated by [Chantler](#)
246 [\(1995\)](#), and then compared to that from the equation of state of pure water (NIST database,
247 [Lemmon et al., 2000](#)). This method provides a direct measurement of the temperature at the
248 beam position; temperature accuracy is better than 5 °C, and temperature varied within less than

249 1 °C during the measurements. Pressure was read from a calibrated Bourdin gauge with a
250 precision better than 5 bars; during the experiment, pressure was maintained within <1 bar by
251 a proportional–integral–derivative (PID) controller system (Bruyère et al., 2008).

252 Yttrium K-edge (17,038 eV) Extended X-ray Absorption Fine Structure (EXAFS) spectra
253 were collected up to 400 °C at 800 bars at the FAME beamline at the European Synchrotron
254 Research Facility (ESRF) in Grenoble, France. The ESRF is a 6.03 GeV ring; operating in 7/8
255 multi-bunch mode it has a maximum current of 200 mA. FAME is a bending magnet beamline
256 (see Proux et al., 2005 for details), and its double crystal Si(220) monochromator provides an
257 energy resolution of 0.87 eV at the Y K-edge energy. A focused beam size of FWHM
258 220 x 145 μm^2 was used. The incident and transmitted beam intensities I_0 and I_1 were measured
259 with Si diodes, and a Canberra 30 element solid state fluorescence detector was used for
260 detecting fluorescence data. The beam energy was calibrated with an Y foil, such that the
261 maximum of the first derivative was at 17,038 eV.

262 2.3.2 XAS data processing

263 EXAFS data were analysed with the HORAE package (Ravel and Newville, 2005), using
264 FEFF version 9 (Rehr et al., 2009); E_0 was defined as the maximum of the first derivative.
265 Reported errors in EXAFS parameters ($1-\sigma$) are those calculated by the Artemis program (part
266 of HORAE). The amplitude reduction factor (S_0^2) accounts for multi-electronic processes that
267 impact the amplitude of the EXAFS signal (Roy et al., 1997), and is determined by fitting a
268 compound with similar molecular structure as the unknown. In our case, S_0^2 was determined
269 by fixing the coordination of a low salinity solution at 30 °C to eight oxygen atoms (Guan et
270 al., 2020), as the structure of the Y(III) aqua ion has been well characterized by previous studies
271 (Ikeda et al., 2005a,b; Ohta et al., 2008; Liu et al., 2012; Lindqvist-Reis et al., 2000). A S_0^2
272 value of 0.73 was determined by refining the S_0^2 , bond lengths and EXAFS Debye-Waller

273 factors for this solution; this value is consistent with theoretical constraints (Roy et al., 1997)
274 and was used in all subsequent refinements.

275 For each solution, all spectra were fitted simultaneously, resulting in one ΔE_0 and one set
276 of goodness-of-fit parameters for each solution. The EXAFS Debye-Waller σ^2 was fitted at the
277 lowest measured temperature for each solution, with the constraint that it typically doubles
278 from 30 to 500 °C, as determined from MD simulations (Guan et al., 2020). Note that the
279 Debye-Waller values determined from the *ab initio* MD simulations are higher than the
280 experimental ones, as a result of the short sampling times in *ab initio* MD, that tend to
281 overestimate structural disorder. However, the relative changes in the MD Debye-Waller
282 values are likely to be accurate, especially since the vibrational characteristics of the complexes
283 are well reproduced by *ab initio* MD (e.g., Mei et al., 2013 and references therein). In practice,
284 this was applied by increasing the EXAFS Debye-Waller by a factor of 1.2 for each ~100 °C
285 increase in temperature. The EXAFS Debye-Waller coefficients for sulfur and chlorine were
286 assumed to be the same as that for O, in part to reduce the number of variables and in part due
287 to the (usually) low (S±Cl):O ratio meaning that an independent measurement of these
288 parameters was not possible.

289 3 Results

290 3.1 Geometry of Y(III)-sulfate complexes

291 The results of *ab initio* MD of Y sulfate complexes from CP2K are summarized in Table 3.
292 The results from CP2K and CPMD for box 3 (Table 1) are compared in Supplementary
293 Table S1. Both codes predict similar geometries (bond distances and coordination numbers) of
294 the complexes at similar conditions, but more ligand exchange reactions were observed from
295 the CPMD simulation than CP2K. Figure 1 shows snapshots of different Y(III)-sulfate and
296 sulfate-chloride complexes.

297 In general, Y(III) can bond with 1 or 2 oxygen atoms from a SO_4^{2-} group, forming
298 monodentate (Y-S distance at $\sim 3.6 \text{ \AA}$) or bidentate (Y-S distance at $\sim 3.0 \text{ \AA}$) structures
299 (Figures 1a, b). Figure 2 shows the distance between Y(III) and S as a function of simulation
300 time, which reflects the change in the structure of the Y-sulfate complexes. At $200 \text{ }^\circ\text{C}$
301 (Figure 2a), simulation (1a) was launched with the $[\text{Y}(\text{SO}_4)(\text{H}_2\text{O})_9]^+$ structure (in the following
302 text, square bracket are used when the full first-shell coordination is indicated, i.e. including
303 coordinated water molecules); for the first 20.5 ps, the complex stabilized as $[\text{Y}(\text{SO}_4)(\text{H}_2\text{O})_{6.6}]^+$
304 with a monodentate SO_4^{2-} . After this, a second sulfate bonded with Y(III), and this $\text{Y}(\text{SO}_4)_2^-$
305 complex was stable for the rest of the simulation. The two sulfate ions were bonded with Y(III)
306 in a monodentate configuration for 41.6 ps, then in the last 19.9 ps one of the sulfate ligands
307 switched to bidentate bonding, which resulted in the loss of one of the coordinated water
308 molecules and decreased the average hydration number of the $\text{Y}(\text{SO}_4)_2^-$ complex from 5.2 to
309 4.2. At $300 \text{ }^\circ\text{C}$ (1b), the simulation started with the configuration $[\text{Y}(\text{SO}_4)(\text{H}_2\text{O})_8]^+$, with
310 bidentate bonding of the sulfate ligands. This configuration remained stable for the whole
311 simulation time (43 ps), with an average hydration number of 7.2.

312 At $350 \text{ }^\circ\text{C}$, in simulation (1c) (Figure 2b), the initial configuration $[\text{Y}(\text{SO}_4)_2(\text{H}_2\text{O})_7]^-$
313 dehydrated rapidly to $[\text{Y}(\text{SO}_4)_2(\text{H}_2\text{O})_{3.8}]^-$ and was then stable for 31.5 ps until another SO_4^{2-}
314 bonded with Y(III) and the hydration number decreased to 1.8. When bonded with two sulfate
315 ions, all three combinations of structures with two sulfate ions were observed (i.e. both sulfate
316 groups in monodentate configuration; both in bidentate configuration; and mixed mono- and
317 bidentate). When Y(III) was bonded to 3 sulfate ions after 30 ps, the 2x bidentate plus 1x
318 monodentate was the predominate configuration.

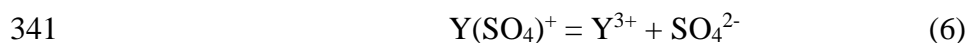
319 Cl^- was then added to the simulation to test for mixed $\text{SO}_4^{2-}\text{-Cl}^-$ complexes (jobs 2a, 2b,
320 2c). Under these conditions, Y-Cl bonding was detected at temperatures over $200 \text{ }^\circ\text{C}$ (350 and
321 $500 \text{ }^\circ\text{C}$). At $200 \text{ }^\circ\text{C}$, simulation (2a, Figure 2c) had a starting configuration of

322 $[Y(SO_4)Cl(H_2O)_7]^0$, which rapidly changed to $[Y(SO_4)(H_2O)_{5.8}]^+$ and then remained stable for
 323 the rest of the simulation. The $Y-SO_4^{2-}$ complex was monodentate but became bidentate for the
 324 last 2 ps of the simulation. At the higher temperatures of 350 and 500 °C (simulations **2b**,
 325 **Figure 2d** and **2c**, **Figure 2e**, respectively), Y(III) was coordinated to both Cl^- and SO_4^{2-} , with
 326 Y-Cl bond lengths ranging from 2.60 Å to 2.63 Å. At 350 °C, the SO_4^{2-} bonded to Y(III)
 327 predominantly in a monodentate manner (**Figure 2d**), whereas it was bidentate at 500 °C
 328 (**Figure 2e**). Deprotonation occurred in both simulations **2b** and **2c**, which resulted in the
 329 formation of $[YCl(HSO_4)(OH)(H_2O)_3]^0$ and $[YCl_2(SO_4)(OH)(H_2O)]^{2-}$ at 350 °C and 500 °C,
 330 respectively (**Figure 1c,1d**). The H^+ in simulation **2c** bonded with the free sulfate and became
 331 HSO_4^- in the simulation box.

332 The hydration number of Y(III) decreased with increasing temperature, with Y-O(H_2O)
 333 distances ranging from 2.32 Å to 2.41 Å. These Y-O(H_2O) distances are slightly longer than
 334 the Y-O(SO_4^{2-}) distances, which range from 2.23 – 2.32 Å. The transition from monodentate
 335 to bidentate sulfate geometry is associated with the loss of one coordinated water, causing a
 336 decrease in hydration number. Deprotonation and formation of Y-OH bonds were also
 337 observed, with Y-OH distances at ~2.10 Å.

338 3.2 *Ab initio* thermodynamic integration of Y(III)-sulfate complexes

339 **Figure 3** shows the results of the free energy surface calculations for the ligand dissociation
 340 reaction of the Y(III) mono-sulfate complex at 200 °C, 800 bar.



342 The Helmholtz free energy $\Delta A_{I \rightarrow II}$ of reaction (6) was calculated by integrating the mean force
 343 (F_C) required to constrain Y-S(SO_4^{2-}) distances at fixed values from position I (average binding
 344 distance for the sulfate in the bidentate $Y(SO_4)^+$ complex, derived from unconstrained MD) to
 345 position II (negligible interactions between the Y(III) and sulfate ions). As expected, F_C is near
 346 zero at both position I ($r_I = 3$ Å; $F_C = 6.4 \pm 2.7$ kJ/(mol·Å)) and II ($r_{II} = 6$ Å; $F_C = -3.1$

347 ± 2.3 kJ/(mol \cdot Å). A second (meta-stable) equilibrium point is found at the intermediate
348 position III (3.6 Å; [Figure 3](#)), which corresponds to the monodentate Y(SO₄)⁺ complex. Thus,
349 a second Helmholtz free energy can be obtained from this calculation, which refers to the
350 change of Y(SO₄)⁺ from the monodentate to bidentate structures ($\Delta A_{I \rightarrow III}$). During the
351 transition from bidentate (position I) to monodentate (position III), F_C reaches a minimum of
352 -64.6 ± 5.7 kJ/(mol \cdot Å) at a Y-S(SO₄²⁻) distance $r = 3.2$ Å. With the increasing Y-S distance
353 from bidentate to monodentate, one of the oxygens from the SO₄²⁻ remains at ~ 2.3 Å, however,
354 the other oxygen moves away from Y(III). For example, at the Y-S(SO₄²⁻) distance of 3.3 Å
355 (position a in [Figure 3](#)), the other oxygen is at 3 Å from Y(III) and the structure became
356 monodentate afterwards, where the hydration number of Y(III) increased by 1 (total hydration
357 number of 6) and reached equilibrium at r_{III} . The difference in the free energy between bi- and
358 mono-dentate Y(SO₄)⁺ is 6.1 ± 3.2 kJ/mol (from r_I to r_{III}). From r_{III} to r_{II} , the maximum energy
359 barrier of dissociation was reached at 4.3 Å (38.1 ± 6.7 kJ/mol). The F_C are close to zero when
360 the Y-S(SO₄²⁻) distance is beyond ~ 5 Å (1.0 ± 2.8 kJ/(mol \cdot Å) at 5.3 Å; 2.3 ± 3.0 kJ/(mol \cdot Å) at
361 5.6 Å and -3.1 ± 2.3 kJ/(mol \cdot Å) at 6.0 Å), indicating that there are no interactions between
362 Y(III) and SO₄²⁻. The integration of F_C over the reaction path gives a free energy difference for
363 reaction (6) of 23.8 ± 12.5 kJ/mol and 17.8 ± 8.9 kJ/mol for bidentate and monodentate
364 Y(SO₄)⁺ complexes, respectively.

365 To test the effect of the box size on the results of the thermodynamic integrations, the free
366 energy surface calculation of reaction (6) at 300 °C was conducted using the box 1 composition
367 ([Table 1](#)), which contains twice as many waters as box 3 (111 vs. 55). Since the CPMD
368 calculations are prohibitively CPU intensive at this box size ($\sim 14,400$ CPU hour for each ps of
369 real time simulation), we reduced the minimum simulation time to ~ 5 ps (instead of 7 ps) at
370 each distance. Still, this single thermodynamic integration run costed a total of ~ 1.76 M CPU
371 hours. All free energy surfaces for the dissociations of the Y(SO₄)⁺ and Y(SO₄)₂⁻ complexes

372 obtained in this study are shown in [Figure 4](#), and the resulting Gibbs free energy of reaction
373 and equilibrium constants for the formation ($\log K$) of these complexes are summarized in
374 [Table 4](#). The results from the two different box sizes are consistent after the concentration and
375 activity correction.

376 Because of the large size of the Y(III)-sulfate complexes ([Fig. 1](#)), the symmetrically
377 equivalent Y-sulfate complexes are separated by ~ 3 water molecules in the boxes containing
378 55 waters. Hence, finite size effects may be significant, but cannot be avoided given current
379 computational capabilities for the *ab initio* approach chosen in this study. Yet, we can be
380 confident that the results presented are valid because the energy of dissociation is expected to
381 be dominated by first-shell effects (sulfate ligand bonding and hydration shell), that are well
382 described via *ab initio* MD even in a small box. This assumption is validated by comparing
383 (i) results of *ab initio* thermodynamic MD in boxes of different sizes, and (ii) results of
384 classical and *ab initio* MD. (i) The thermodynamic properties derived from the simulations in
385 boxes with 55 vs. 111 waters are equal within error. The doubling of the number of atoms
386 results in a factor 10 increase in computational resources, but only 26% increase in the linear
387 box size; however, the separation between the symmetrically equivalent Y-sulfate complexes
388 increases significantly by at least one water molecule in the boxes containing 111 waters
389 compared to 55 waters ([Table 1](#); box length increases by 3.37 Å). Hence, the results from the
390 larger box confirm the dominance of first shell effects on the energetics of the ligand formation
391 reactions. (ii) Classical MD employing the potential mean force (PMF) can be conducted in
392 large simulation boxes (1000's of water molecules), minimizing the effects of box size and
393 ionic strength. However, empirical potential parameters are usually based on the experimental
394 and *ab initio* results, and are poorly suited to quantify first-shell interactions, especially in
395 systems with complex orbital shapes imposing strong constraints on the geometry of the
396 complexes. In the case of REE, [Zhang and Yan \(2022\)](#) recently showed that these limitations

397 reduce the accuracy of thermodynamic predictions for ligand exchange reactions; for example,
398 the $\log\beta$ of $\text{La}(\text{SO}_4)^+$ calculated from classical MD at 250 °C is 3.69 ± 0.06 higher than the
399 experimentally-based value (Migdisov et al. 2016). Finally, direct comparison with
400 experimental data is important to validate the predicted geometry and stoichiometry of the
401 complexes; in this study, we find excellent qualitative agreement between *ab initio* simulations
402 and *in-situ* XAS results.

403 3.3 Extended X-ray Absorption Fine Structure Spectroscopy (EXAFS)

404 Two sets of solutions were measured (Table 2); sulfate-only (Sols 2,4,10) and mixed
405 sulfate-chloride solutions (Sols 9,13,14). All R-space spectra have a peak at ~ 1.9 Å (phase
406 uncorrected) due to Y-O bonding, and some solutions show a small peak at ~ 2.5 Å (phase
407 uncorrected) due to Y-S bonding (Figure 5). The Y-O peak (i) shifted position slightly with
408 temperature and (ii) showed the ‘classic’ dehydration effect for metal complexes, where the
409 number of O atoms (i.e. waters of hydration) coordinated to Y(III) decreased with increasing
410 temperature (Table 5, Figure 5; Brugger et al. 2016). In contrast, the Y-S(SO_4^{2-}) peak position
411 remained constant with temperature (Figure 5b).

412 EXAFS cannot distinguish between oxygen from water or from a sulfate group, as the Y-
413 O contribution can be fitted with a single average distance (Figure 5), but the experimental Y-
414 O distances (2.32 to 2.385 Å) are close to the average distances derived from MD, which results
415 show that Y-O(H_2O) distances generally range from 2.38 to 2.40 Å, whereas Y-O(SO_4^{2-})
416 distances range from 2.23 to 2.32 Å. For example for Sol4 (~ 2 m SO_4^{2-} Table 2, comparable to
417 MD job 1a, Table 3) at 200 °C, the experimental bond length (2.368(7) Å) is similar to the
418 averaged MD Y-O(H_2O) and Y-O(SO_4^{2-}) bond lengths for the first 20 ps, ~ 2.37 Å; the MD
419 water-sulfate Y-O bond length averaged over 80 ps is ~ 2.35 Å, which is within $3\text{-}\sigma$ of the
420 experimentally derived bond length. At 350 °C, the experimental Y-O bond length is
421 2.357(7) Å, which is within $2\text{-}\sigma$ of the average MD value ~ 2.35 Å.

422 EXAFS fits (Figure 5) of the sulfate-only solutions demonstrated that Y-S complexing
423 only occurred for the higher pH solutions, i.e. where most of the sulfate was introduced as
424 Na_2SO_4 with only minor H_2SO_4 to acidify the solution to avoid hydroxide complexing
425 (Table 2). No Y(III) sulfate complexing was observed in low pH solutions, where H_2SO_4 was
426 the only source of sulfate. As noted in section 3.1, MD simulations indicate that monodentate
427 Y-S distances are ~ 3.6 Å and bidentate Y-S distances ~ 3.0 Å (Figure 1a,b). Thus, based on the
428 experimentally fitted bond length (2.98 to 3.08 Å, Table 5), it can be determined that the Y(III)-
429 sulfate complexes are predominantly bidentate. The bidentate coordination resulted in a
430 relatively rigid structure, and while some Y-S(SO_4^{2-}) bond lengths had to be fixed for the
431 EXAFS refinement, it can be seen that the Y-S(SO_4^{2-}) peak position does not shift with
432 temperature (Figure 5b).

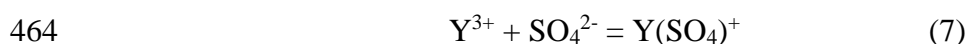
433 EXAFS fits of the mixed sulfate-chloride solutions indicated that Y(III) chloride
434 complexing occurred in all solutions where Cl^- was present (Sols9,13,14). In Sol9, there was
435 no Y(III) sulfate complexing as H_2SO_4 was the only source of sulfate, and the number of
436 chloride bonding to Y(III) increased slightly with increasing temperature [$\text{Y}(\text{H}_2\text{O})_{7.1}\text{Cl}_{1.3}$ at
437 30°C to $\text{Y}(\text{H}_2\text{O})_{5.0}\text{Cl}_{1.6}$ at 350°C], an observation that is consistent with many previous studies
438 of metal-chloride complexing (e.g., Brugger et al. 2016; Crerar et al. 1985; Guan et al. 2020;
439 Liu et al. 2011; Mei et al. 2015a). For solutions that had Y(III) complexing with both SO_4^{2-} and
440 Cl^- (Sol13,14), the number of sulfate bonded to Y(III) increased slightly with increasing
441 temperature, while the number of chlorides decreased [$\text{Y}(\text{H}_2\text{O})_{4.8}\text{Cl}_{1.8}(\text{SO}_4)_{1.3}$ at 200°C to
442 $\text{Y}(\text{H}_2\text{O})_{4.3}\text{Cl}_{1.3}(\text{SO}_4)_{1.6}$ at $350\text{-}400^\circ\text{C}$, Sol13]. This is in apparent contradiction to the MD
443 results, which demonstrated increasing Y-Cl coordination with increasing temperature (no Y-
444 Cl complexing at 200°C , even when Cl was included in the initial configuration and increasing
445 Y-Cl coordination at 500°C , as described in section 3.1). However, direct comparison is
446 difficult, because the pH in the experiments changes from acidic at room T to near neutral at

447 400 °C (Table 2), which is expected to decrease chloride complexing versus sulfate complexing.
448 With respect to the geometry of the predominant complexes, the experimental and MD results
449 agree well: the Y-Cl bond lengths are similar, being within 3σ of the experimental error (2.68(1)
450 to 2.76(7) Å experimental and 2.60 to 2.63 Å MD). Importantly, both experimental and MD
451 results agree that Y-sulfate coordination increases with increasing temperature in these mixed
452 sulfate-chloride solutions.

453 4 Discussion

454 4.1 Y(III)-sulfate complexes : monodentate vs. bidentate

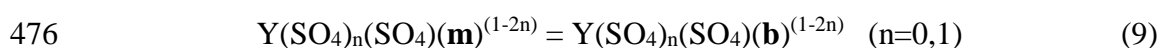
455 Ligands like sulfate and carbonate can form both monodentate or bidentate structures
456 (Brugger et al., 2016), which affects the geometry and stability of metal complexes in
457 hydrothermal fluids (e.g., UO_2^{2+} -sulfate, Kalintsev et al., 2019; and Eu(III)-sulfate, Liu et al.,
458 2017). The unconstrained MD results show that Y(III) can bond with SO_4^{2-} in both
459 monodentate and bidentate modes; therefore, when bonding with two (or more) SO_4^{2-} , the
460 configuration can be any combination of monodentate, bidentate or mixed structures.
461 Thermodynamic integration provides an effective way to determine the formation constants
462 and the difference in Gibbs free energy between the two structures. The results are summarized
463 in Table 6. For the reactions:



466 at the same conditions, the maximum absolute difference of the Gibbs free energy between the
467 two structures (mono and bidentate for reaction (7); 1x monodentate and 1xbidentate, and
468 2xbidentate for reaction (8), Table 6) is -14.0 ± 3.4 kJ/mol for reaction (8) at 300 °C (800 bar).
469 Previous theoretical calculations of uranyl sulfate (Vallet and Grenthe, 2007) at 25 °C had

470 similar differences in Gibbs free energies from monodentate to bidentate of -17 kJ/mol for
471 $\text{UO}_2(\text{SO}_4)$ and -13 kJ/mol for $\text{UO}_2(\text{SO}_4)_2^{2-}$, respectively.

472 The studies of both Y(III)- and uranyl- mono-/bidentate sulfate complexes suggest that in
473 general the bidentate structures are slightly more stable than the monodentate structure.
474 However, for reaction (8) at 200 °C, calculations show that near-equal amounts of monodentate
475 and bidentate Y-sulfate structures could exist in the solution. For the equilibrium:

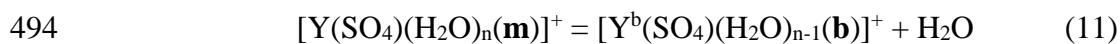


477 where (m) indicates monodentate, and (b) bidentate sulfate complexing; the corresponding
478 mass action equation is

$$479 \quad \ln(K_9) = -\frac{\Delta_r G}{RT} = \ln \frac{a_{\text{Y}(\text{SO}_4)_n(\text{SO}_4)(\mathbf{b})^{(1-2n)}}}{a_{\text{Y}(\text{SO}_4)_n(\text{SO}_4)(\mathbf{m})^{(1-2n)}}} = \ln \frac{c_{\text{Y}(\text{SO}_4)_n(\text{SO}_4)(\mathbf{b})^{(1-2n)}} \gamma_{\text{Y}(\text{SO}_4)_n(\text{SO}_4)(\mathbf{b})^{(1-2n)}}}{c_{\text{Y}(\text{SO}_4)_n(\text{SO}_4)(\mathbf{m})^{(1-2n)}} \gamma_{\text{Y}(\text{SO}_4)_n(\text{SO}_4)(\mathbf{m})^{(1-2n)}}} \quad (10)$$

480 Because the activity coefficients for both isomers are identical (same charges of the
481 species), equation (10) provides the actual ratio of the two isomers $\left(\frac{c_{\text{Y}(\text{SO}_4)_n(\text{SO}_4)(\mathbf{b})^{(1-2n)}}}{c_{\text{Y}(\text{SO}_4)_n(\text{SO}_4)(\mathbf{m})^{(1-2n)}}}\right)$ as a
482 function of Gibbs free energy of reaction ($\Delta_r G$) and temperature (T, in kelvin); the ratio is 1 if
483 $\Delta_r G=0$ at all temperature; at 200°C, the ratio is 0.8 at $\Delta_r G= -1$ kJ/mol, and 4.6 at $\Delta_r G= -$
484 6 kJ/mol; at 300°C, the ratios is 1.5 at $\Delta_r G = -2$ kJ/mol and 18.9 at $\Delta_r G = -14$ kJ/mol; at 400°C,
485 the ratios are 6.0 at $\Delta_r G = -10$ kJ/mol and 2.4 at $\Delta_r G = -5$ kJ/mol (Table 6).

486 The EXAFS analysis confirms that at temperatures over 200 °C, Y(III) sulfate complexes
487 are predominantly bidentate. A previous *in situ* XAS study on Eu(III) (Liu et al., 2017) found
488 a similar bidentate configuration for the $\text{Eu}(\text{SO}_4)_2^{2-}$ complex, and it can thus be expected that
489 all REE will form similar complexes in S-bearing hydrothermal fluids. The trends of higher
490 translational entropy with increasing temperatures of the system (Mei et al., 2015a; Brugger et
491 al., 2016) is one of the reasons to favour the bidentate structure of Y(III)- $(\text{SO}_4^{2-})_{1,2}$ complexes,
492 as the second oxygen of the bonded sulfate will substitute for one water molecule when the
493 structure changes from monodentate to bidentate, e.g.



495 Therefore, considering the experimental results, the bidentate formation constants of each
496 reaction are chosen as the final data for geochemical modelling. The cumulative formation
497 constant ($\log\beta$) of each reaction at different P-T are listed in [Table 7](#).

498 4.2 Thermodynamic extrapolations

499 The thermodynamic properties of all predominant aqueous species are required over a
500 wide range of temperatures and pressures to enable predictions of metal transport and
501 precipitation under hydrothermal conditions, in particular simulations of complex processes
502 such as fluid-rock interaction, fluid mixing, or cooling. The HKF equation-of-state is the most
503 widely used semi-empirical EOS to extrapolate the thermodynamic properties of aqueous
504 complexes from limited experiment points. The original HKF EOS is applicable to 1000 °C
505 and 5 kbar, and recently the approach has been extended to 6.0 GPa and 1200 °C ([Sverjensky](#)
506 [et al. 2014](#); [Huang and Sverjensky, 2019](#)).

507 In this study, we fitted the HKF EOS for the standard Gibbs free energy of formation from
508 the elements ($\Delta_f G^0(P, T)$) for the YSO_4^+ and $\text{Y}(\text{SO}_4)_2^-$ complexes described here, as well as
509 for the YCl_n^{3-n} ($n=1-4$) complexes studied by [Guan et al. \(2020\)](#). The fitting strategy was
510 optimised to reflect most of the available constraints of Y-sulfate and Y-chloride complexing,
511 and minimise the number of empirical fit parameters. The $\Delta_f G^0(P, T)$ each aqueous species
512 were calculated from their formation constants and $\Delta_f G^0(P, T)$ values of Y^{3+} , SO_4^{2-} and Cl^-
513 computed with HKF parameters compiled by [Shock & Helgeson \(1988\)](#) and [Shock et al. \(1997\)](#).

514 For Y-sulfate complexes, we fitted $\Delta_f G^0(P, T)$ at 200, 300 and 400 °C and 800 bar ([Table 7](#))
515 from MD; assuming that the REE-sulfate complexes behave coherently in hydrothermal fluids
516 ([Migdisov et al., 2016](#); [Cangelosi et al., 2020](#)), the experimental values of $\text{Er}(\text{SO}_4)_n^{3-2n}$ ($n=1,2$)
517 from [Migdisov and Williams-Jones \(2008\)](#) at 25°C, 100°C, 150°C, 200°C and 250°C (at P_{sat})
518 were also included in the fitting to provide a model that is internally consistent with REE. The

519 data at 200 °C, Psat of $\text{Er}(\text{SO}_4)_n^{3-2n}$ ($n=1,2$) from Migdisov and Williams-Jones (2008) is within
520 the error of the data of $\text{Y}(\text{SO}_4)_n^{3-2n}$ ($n=1,2$) in this study at 200 °C, 800 bar. Y+REE speciation
521 in seawater was recently reviewed by Schijf and Byrne (2021), who provided a $\log K_{25^\circ\text{C}}$ for
522 the formation of YSO_4^+ of 3.50, similar to the value of 3.59 ± 0.11 for ErSO_4^+ of Migdisov and
523 Williams-Jones (2008).

524 For Y-chloride complexes, $\Delta_f G^0(25^\circ\text{C}, 1\text{bar})$ of YCl_n^{3-n} ($n= 1, 2$) was set to the values
525 from the thermodynamic parameters of Ho-Cl complexes from the study of Migdisov et al.,
526 (2009); values for $n=3,4$ were estimated assuming a linear behaviour of the energetics of the
527 step-wise complex forming reactions. Similar to Y-sulfate, the formation constant for the YCl^{2+}
528 complex reported by Schijf and Byrne (2021) (0.65 ± 0.03) is identical within error to the value
529 for HoCl^{2+} of 0.71 derived from Migdisov et al. (2009). The partial molar volume
530 ($\bar{V}^0(25^\circ\text{C}, 1\text{bar})$) of the sulfate and chloride complexes were chosen from the linear
531 correlations as from Haas et al. (1995).

532 Within the HKF formalism, the pressure and temperature dependence of the partial molar
533 volume ($\bar{V}^0(25^\circ\text{C}, 1\text{bar})$) and molar heat capacity ($\bar{c}_p^0(25^\circ\text{C}, 1\text{bar})$) are described by the
534 empirical parameters $a1$ - $a4$ and $c1$ - $c2$, respectively. We attempted to use the empirical
535 correlations proposed in the DEW model of Sverjensky et al. (2014) for these parameters, i.e.,
536 fitting only $\Delta_f G^0(25^\circ\text{C}, 1\text{bar})$, molar entropy ($\bar{S}^0(25^\circ\text{C}, 1\text{bar})$), $\bar{c}_p^0(25^\circ\text{C}, 1\text{bar})$, and, for
537 sulfate complexes, $\bar{V}^0(25^\circ\text{C}, 1\text{bar})$; however, we found that this approach did not reproduce
538 the selected data points within 2σ error. For the final fits, reported in Table 8, we therefore fit
539 the PT dependence of (i) molar volume using the $a1$ parameter ($a2=a3=a4=0$; refining these
540 did not improve the results significantly), and (ii) molar heat capacity using $c1$ and $c2$. The
541 Born coefficient ω was calculated using the correlations defined in the DEW model
542 (Sverjensky et al. 2014). Optimisation was conducted using a non-linear least square approach

543 to minimise the sum of the square of the predicted and experimental $\Delta_f G^0(P, T)$, weighted by
544 the experimental errors of each datapoint.

545 The parameters of the HKF EOS provided in Table 8 should be considered as provisional
546 and will be refined in subsequent publications.

547 4.3 Geological implications

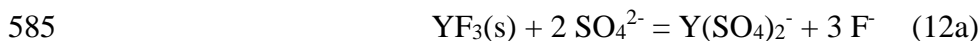
548 Our *ab initio* thermodynamic integration provided formation constants of Y(III) sulfate
549 complexes up to high temperatures (400 °C). Together with the thermodynamic data of Y(III)
550 chloride (Table 8), Y(III) fluoride (Dos Santos et al., 2012; Loges et al., 2013) and Y(OH)₃(s)
551 (Navrotsky et al., 2015), it is now possible to model the Y solubility and the predominant Y(III)
552 species in hydrothermal sulfate, chlorine and fluorine fluids. The modelling was conducted
553 with the CHNOSZ program (Dick, 2019). The thermodynamic data for aqueous species other
554 than Y(III) are sourced from its default OBIGT database, which includes the aqueous species
555 from Sverjensky et al. (1997). Thermodynamic data for Y³⁺ and hydroxide Y(III) complexes
556 in OBIGT are sourced from Shock and Helgeson (1998) and Shock et al. (1997).

557 Figure 6 shows the predominant species of Y(III) in the Cl⁻-SO₄²⁻-F⁻-Na⁺ system as a
558 function of pH and temperature, for oxidised (sulfate stable), chloride-rich fluids (Cl:S = 10).
559 Fluorine is also present, at concentrations typical of F-rich hydrothermal systems (Cl:F = 200
560 and 2000; Banks et al., 1994; Xing et al. 2019; Yardley, 2005). Y³⁺ is predominant only at low
561 temperature and at low pH, at both P_{sat} (Figures 6a, b) and 1000 bar (Figures 6c, d). Yttrium
562 forms strong complexes with fluorine (Loges et al., 2013), although the mobility of Y+REE in
563 F-rich fluids is limited by the low solubility of fluoride-bearing minerals (e.g., Migdisov, et al.,
564 2019), such as simple fluorides (used as proxies in our simple diagrams) and fluoro-carbonates.
565 In all diagrams, YF₃(s) and Y(OH)₃(s) are the solubility-limiting phases (shown for 1 ppb Y).
566 The stability of Y(III)-Cl complexes increases with increasing temperature, and Y(III) exists
567 predominantly as YCl₃(aq) in the modelled brines (2 molal chloride). Y(III) sulfate complexes

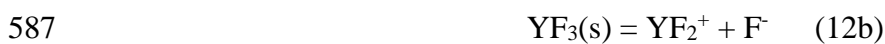
568 may play an important role in Y transport when there is relatively low concentration of fluorine
 569 in the fluids, and $Y(SO_4)_2^-$ is predicted to predominate at temperature from 100 to 300°C over
 570 a pH range of ~1.5 – 4 at P_{sat} (Figure 6b). At pressure of 1 kbar, $Y(SO_4)^+$ is predicted to
 571 predominate at intermediate acidic pH at temperatures from 100 °C to ~180 °C, and at higher
 572 temperature the $Y(SO_4)_2^-$ complex becomes predominant to temperatures of ~280 °C; at higher
 573 temperature, Y-chloride complexes take over (Figure 6d).

574 Hence, the presence of sulfate increases the solubility of Y(III) under specific conditions.
 575 Since the stability of sulfate is redox sensitive, Y(III) solubility becomes highly redox-sensitive,
 576 with rapid precipitation of Y minerals upon destabilisation of aqueous sulfate. Though mix
 577 ligand Y(III)-sulfate-chloride complexes were not included in the geochemical model due to
 578 lack of quantitative data, Y(III) solubility may be further increased by the formation of Y(III)-
 579 sulfate-chloride.

580 An interesting feature of the diagrams in Figures 6 is the strong effect of pressure on
 581 mineral solubility and aqueous Y(III) speciation. For example, the predominance field of the
 582 aqueous Y-F complex increases dramatically at 1 kbar versus P_{sat} , resulting in a significant
 583 increase in Y solubility via reaction (12b) compared to (12a). This difference suggests that
 584 reactions (12a) and (12b) are associated with large changes in molar volumes:



586
$$\Delta_r \bar{V}_{25^\circ C, 1bar}^0 = -53.8 \text{ cm}^3 \text{ mol}^{-1}; \Delta_r \bar{V}_{200^\circ C, 1000bar}^0 = -71.0 \text{ cm}^3 \text{ mol}^{-1}$$



588
$$\Delta_r \bar{V}_{25^\circ C, 1bar}^0 = -130.1 \text{ cm}^3 \text{ mol}^{-1}; \Delta_r \bar{V}_{200^\circ C, 1000bar}^0 = -136.73 \text{ cm}^3 \text{ mol}^{-1}$$

589 The main reason for these differences is that the fluoride and sulfate ions have different
 590 hydration spheres (e.g., Patel et al., 2011). Such strong pressure effects on aqueous speciation
 591 are rarely reported in the literature, and usually expected over larger pressure differences (e.g.,
 592 Brugger et al. 2016; Ohoa, et al., 2015). Hence, the simulation results suggest that in cases

593 involving ligand exchange among halides and oxyanion ligands such as sulfate and carbonate,
594 pressure may have a significant effect at mid- to upper-crustal depths, and that pressure-
595 induced precipitation may be a significant ore-forming process in some cases.

596 Acknowledgements

597 We thank Sandro Jahn and anonymous reviewers for providing insightful reviews, and
598 Associate Editor Xiandong Liu for handling the manuscript. We thank Ignacio González-
599 Álvarez and Fang Huang for their suggestions that improved the manuscript. Research funding
600 is provided by the Australian Research Council (ARC discovery grant DP190100216), Monash
601 University scholarship to Q.G., and CSIRO Deep Earth Imaging Future Science Platform to
602 YM. The MD simulation of this work was supported by resources provided by the Pawsey
603 Supercomputing Centre with funding from the Australian Government and the Government of
604 Western Australia, the National Computational Infrastructure (NCI) supported by the
605 Australian Government, and the high-performance computers in CSIRO. We are grateful to the
606 European Synchrotron Research Facility (Grenoble, France) for providing beamtime, and to
607 the Australian International Synchrotron Access Program (ISAP) managed by the Australian
608 Synchrotron, part of ANSTO, and funded by the Australian Government, for travel funding.
609 Evgeniy Bastrakov publishes with the permission of the CEO, Geoscience Australia.

610 References

- 611 Allen, M. and Tildesley, D. (1987) *Computer Simulation of Liquids*. Oxford University Press,
612 Oxford, UK.
- 613 Bach, W., Roberts, S., Vanko, D.A., Binns, R.A., Yeats, C.J., Craddock, P.R. and Humphris,
614 S.E. (2003) Controls of fluid chemistry and complexation on rare-earth element contents
615 of anhydrite from the Pacmanus subseafloor hydrothermal system, Manus Basin, Papua
616 New Guinea. *Mineralium Deposita* 38, 916-935.

617 Banks, D.A., Yardley, B.W.D., Campbell, A.R. and Jarvis, K.E. (1994) REE composition of
618 an aqueous magmatic fluid: A fluid inclusion study from the Capitan Pluton, New Mexico,
619 U.S.A. *Chemical Geology* 113, 259-272.

620 Bastrakov, E.N., Skirrow, R.G. and Davidson, G.J. (2007) Fluid Evolution and Origins of Iron
621 Oxide Cu-Au Prospects in the Olympic Dam District, Gawler Craton, South Australia.
622 *Economic Geology* 102, 1415-1440.

623 Becke, A.D. (1988) Density-functional exchange-energy approximation with correct
624 asymptotic behavior. *Physical Review A* 38, 3098-3100.

625 Brugger, J., Etschmann, B., Pownceby, M., Liu, W., Grundler, P. and Brewe, D. (2008)
626 Oxidation state of europium in scheelite: tracking fluid-rock interaction in gold deposits.
627 *Chemical Geology* 257, 26-33.

628 Brugger, J., Liu, W., Etschmann, B., Mei, Y., Sherman, D.M. and Testemale, D. (2016) A
629 review of the coordination chemistry of hydrothermal systems, or do coordination changes
630 make ore deposits? *Chemical Geology* 447, 219-253.

631 Bruyère, R., Prat, A., Goujon, C. and Hazemann, J.-L. (2008) A new pressure regulation device
632 using high pressure isolation valves, *Journal of Physics: Conference Series*. IOP
633 Publishing, p. 122003.

634 Cangelosi, D., Smith, M., Banks, D. and Yardley, B. (2020) The role of sulfate-rich fluids in
635 heavy rare earth enrichment at the Dashigou carbonatite deposit, Huanglongpu, China.
636 *Mineralogical Magazine* 84, 65-80.

637 Car, R. and Parrinello, M. (1985) Unified Approach for Molecular Dynamics and Density-
638 Functional Theory. *Physical Review Letters* 55, 2471-2474.

639 Chantler, C.T. (1995) Theoretical form factor, attenuation, and scattering tabulation for Z= 1–
640 92 from E= 1–10 eV to E= 0.4–1.0 MeV. *Journal of Physical and Chemical Reference*
641 *Data* 24, 71-643.

642 Crerar, D., Wood, S. and Brantley, S. (1985) Chemical controls on solubility of ore-forming
643 minerals in hydrothermal solutions. *Canadian Mineralogist* 23, 333-352.

644 Cui, H., Zhong, R., Xie, Y., Yuan, X., Liu, W., Brugger, J. and Yu, C. (2020) Forming sulfate-
645 and REE-rich fluids in the presence of quartz. *Geology* 48, 145-148.

646 Debret, B. and Sverjensky, D. (2017) Highly oxidising fluids generated during serpentinite
647 breakdown in subduction zones. *Scientific reports* 7, 1-6.

648 Dick, J.M. (2019) CHNOSZ: Thermodynamic calculations and diagrams for geochemistry.
649 *Frontiers in Earth Science* 7, 180.

650 Dos Santos, I.A., Klimm, D., Baldochi, S.L. and Ranieri, I.M. (2012) Thermodynamic
651 modeling of the LiF–YF₃ phase diagram. *Journal of Crystal Growth* 360, 172-175.

652 Driesner, T. (2007) The system H₂O–NaCl. Part II: Correlations for molar volume, enthalpy,
653 and isobaric heat capacity from 0 to 1000°C, 1 to 5000bar, and 0 to 1 XNaCl. *Geochimica
654 et Cosmochimica Acta* 71, 4902-4919.

655 Driesner, T. and Heinrich, C.A. (2007) The system H₂O–NaCl. Part I: Correlation formulae
656 for phase relations in temperature–pressure–composition space from 0 to 1000°C, 0 to
657 5000bar, and 0 to 1 XNaCl. *Geochimica et Cosmochimica Acta* 71, 4880-4901.

658 Etschmann, B., Liu, W., Mayanovic, R., Mei, Y., Heald, S., Gordon, R. and Brugger, J. (2019)
659 Zinc transport in hydrothermal fluids: On the roles of pressure and sulfur vs. chlorine
660 complexing. *American Mineralogist: Journal of Earth and Planetary Materials* 104, 158-
661 161.

662 Fay, D.P., Litchinsky, D. and Purdie, N. (1969) Ultrasonic absorption in aqueous salts of the
663 lanthanides. *The Journal of Physical Chemistry* 73, 544-552.

664 Gimeno Serrano, M.a.J., Auqué Sanz, L.F. and Nordstrom, D.K. (2000) REE speciation in low-
665 temperature acidic waters and the competitive effects of aluminum. *Chemical Geology*
666 165, 167-180.

667 Goedecker, S., Teter, M. and Hutter, J. (1996) Separable dual-space Gaussian pseudopotentials.
668 Physical Review B 54, 1703-1710.

669 González-Álvarez, I., Stoppa, F., Yang, X. Y., & Porwal, A. (2021). Introduction to the Special
670 Issue, Insights on Carbonatites and their Mineral Exploration approach: A Challenge
671 towards Resourcing Critical Metals. Ore Geology Reviews, 104073.

672 Guan, Q., Mei, Y., Etschmann, B., Testemale, D., Louvel, M. and Brugger, J. (2020) Yttrium
673 complexation and hydration in chloride-rich hydrothermal fluids: A combined ab initio
674 molecular dynamics and in situ X-ray absorption spectroscopy study. Geochimica et
675 Cosmochimica Acta 281, 168-189.

676 Haas, J.R., Shock, E.L. and Sassani, D.C. (1995) Rare earth elements in hydrothermal systems:
677 Estimates of standard partial molal thermodynamic properties of aqueous complexes of
678 the rare earth elements at high pressures and temperatures. Geochimica et Cosmochimica
679 Acta 59, 4329-4350.

680 Hartwigsen, C., Goedecker, S. and Hutter, J. (1998) Relativistic separable dual-space Gaussian
681 pseudopotentials from H to Rn. Physical Review B 58, 3641-3662.

682 Helgeson, H.C. and Kirkham, D.H. (1974) Theoretical prediction of the thermodynamic
683 behavior of aqueous electrolytes at high pressures and temperatures; II, Debye-Huckel
684 parameters for activity coefficients and relative partial molal properties. American Journal
685 of Science 274, 1199-1261.

686 Helgeson, H.C., Kirkham, D.H. and Flowers, G.C. (1981) Theoretical prediction of the
687 thermodynamic behavior of aqueous electrolytes by high pressures and temperatures; IV,
688 Calculation of activity coefficients, osmotic coefficients, and apparent molal and standard
689 and relative partial molal properties to 600°C and 5kb. American Journal of Science 281,
690 1249-1516.

691 Humphrey, W., Dalke, A. and Schulten, K. (1996) VMD: Visual molecular dynamics. Journal
692 of Molecular Graphics 14, 33-38.

693 Huang, F. and Sverjensky, D.A. (2019) Extended Deep Earth Water Model for predicting major
694 element mantle metasomatism. *Geochimica Et Cosmochimica Acta* 254, 192-230.

695 Ikeda, T., Hirata, M. and Kimura, T. (2005a) Hydration of Y^{3+} ion: A Car-Parrinello molecular
696 dynamics study. *The Journal of Chemical Physics* 122, 024510.

697 Ikeda, T., Hirata, M. and Kimura, T. (2005b) Hydration structure of Y^{3+} and La^{3+} compared:
698 An application of metadynamics. *The Journal of chemical physics* 122, 244507.

699 Inguaggiato, C., Censi, P., Zuddas, P., Londoño, J.M., Chacón, Z., Alzate, D., Brusca, L. and
700 D'Alessandro, W. (2015) Geochemistry of REE, Zr and Hf in a wide range of pH and
701 water composition: The Nevado del Ruiz volcano-hydrothermal system (Colombia).
702 *Chemical Geology* 417, 125-133.

703 Jowitt, S.M., Mudd, G.M. and Thompson, J.F. (2020) Future availability of non-renewable
704 metal resources and the influence of environmental, social, and governance conflicts on
705 metal production. *Communications Earth & Environment* 1, 1-8.

706 Kalintsev, A., Migdisov, A., Xu, H., Roback, R. and Brugger, J. (2019) Uranyl speciation in
707 sulfate-bearing hydrothermal solutions up to 250 °C. *Geochimica et Cosmochimica Acta*
708 267, 75-91.

709 Kohn, W. and Sham, L.J. (1965) Self-Consistent Equations Including Exchange and
710 Correlation Effects. *Physical Review* 140, A1133-A1138.

711 Krack, M. (2005) Pseudopotentials for H to Kr optimized for gradient-corrected exchange-
712 correlation functionals. *Theoretical Chemistry Accounts* 114, 145-152.

713 Kühne, T.D., Iannuzzi, M., Del Ben, M., Rybkin, V.V., Seewald, P., Stein, F., Laino, T.,
714 Khaliullin, R.Z., Schütt, O., Schiffmann, F., Golze, D., Wilhelm, J., Chulkov, S., Bani-
715 Hashemian, M.H., Weber, V., Borštnik, U., Taillefumier, M., Jakobovits, A.S., Lazzaro,

716 A., Pabst, H., Müller, T., Schade, R., Guidon, M., Andermatt, S., Holmberg, N., Schenter,
717 G.K., Hehn, A., Bussy, A., Belleflamme, F., Tabacchi, G., Glöß, A., Lass, M., Bethune, I.,
718 Mundy, C.J., Plessl, C., Watkins, M., VandeVondele, J., Krack, M. and Hutter, J. (2020)
719 CP2K: An electronic structure and molecular dynamics software package - Quickstep:
720 Efficient and accurate electronic structure calculations. *The Journal of Chemical Physics*
721 152, 194103.

722 Lee, C., Yang, W. and Parr, R.G. (1988) Development of the Colle-Salvetti correlation-energy
723 formula into a functional of the electron density. *Physical Review B* 37, 785-789.

724 Lemmon E. W., McLinden M. O. and Friend D. G. (2000) Thermophysical properties of fluid
725 systems. National Institute of Standards and Technology, Gaithersberg

726 Lin, I.-C., Seitsonen, A.P., Tavernelli, I. and Rothlisberger, U. (2012) Structure and Dynamics
727 of Liquid Water from ab Initio Molecular Dynamics—Comparison of BLYP, PBE, and
728 revPBE Density Functionals with and without van der Waals Corrections. *Journal of*
729 *Chemical Theory and Computation* 8, 3902-3910.

730 Lindqvist-Reis P., Lamble K., Pattanaik S., Persson I. and Sandström M. (2000) Hydration
731 of the yttrium(III) ion in aqueous solution. An X-ray diffraction and XAFS structural study.
732 *J. Phys. Chem. B* 104, 402–408.

733 Liu, W., Borg, S.J., Testemale, D., Etschmann, B., Hazemann, J.-L. and Brugger, J. (2011)
734 Speciation and thermodynamic properties for cobalt chloride complexes in hydrothermal
735 fluids at 35-440 °C and 600 bar: An in-situ XAS study. *Geochimica Et Cosmochimica*
736 *Acta* 75, 1227-1248.

737 Liu, X., Lu, X., Wang, R. and Zhou, H. (2012) First-principles molecular dynamics study of
738 stepwise hydrolysis reactions of Y³⁺ cations. *Chemical Geology* 334, 37-43.

739 Liu, W., Etschmann, B., Migdisov, A., Boukhalfa, H., Testemale, D., Müller, H., Hazemann,
740 J.-L. and Brugger, J. (2017) Revisiting the hydrothermal geochemistry of europium(II/III)
741 in light of new in-situ XAS spectroscopy results. *Chemical Geology* 459, 61-74.

742 Loges, A., Migdisov, A.A., Wagner, T., Williams-Jones, A.E. and Markl, G. (2013) An
743 experimental study of the aqueous solubility and speciation of Y(III) fluoride at
744 temperatures up to 250°C. *Geochimica et Cosmochimica Acta* 123, 403-415.

745 Louvel, M., Bordage, A., Tripoli, B., Testemale, D., Hazemann, J.-L. and Mavrogenes, J. (2017)
746 Effect of S on the aqueous and gaseous transport of Cu in porphyry and epithermal systems:
747 Constraints from in situ XAS measurements up to 600° C and 300 bars. *Chemical Geology*
748 466, 500-511.

749 Lozano, A., Ayora, C., Macías, F., León, R., Gimeno, M.J. and Auqué, L. (2020) Geochemical
750 behavior of rare earth elements in acid drainages: Modeling achievements and limitations.
751 *Journal of Geochemical Exploration*, 106577.

752 Marshall, W.L. and Franck, E.U. (1981) Ion product of water substance, 0–1000 °C, 1–10,000
753 bars New International Formulation and its background. *Journal of Physical and Chemical*
754 *Reference Data* 10, 295-304.

755 Massari, S. and Ruberti, M. (2013) Rare earth elements as critical raw materials: Focus on
756 international markets and future strategies. *Resources Policy* 38, 36-43.

757 McLemore, V. T. (2011). Geology and mineral deposits of the Gallinas Mountains REE deposit,
758 Lincoln and Torrance Counties, NM; Preliminary report. In SME Annual Meeting, Feb27-
759 Mar02 (pp. 11-139).

760 Mei, Y., Sherman, D.M., Liu, W. and Brugger, J. (2013) *Ab initio* molecular dynamics
761 simulation and free energy exploration of copper(I) complexation by chloride and bisulfide
762 in hydrothermal fluids. *Geochimica et Cosmochimica Acta* 102, 45-64.

763 Mei, Y., Liu, W.H., Sherman, D.M. and Brugger, J. (2014) Metal complexation and ion
764 hydration in low density hydrothermal fluids: Ab initio molecular dynamics simulation of
765 Cu(I) and Au(I) in chloride solutions (25-1000 °C, 1-5000 bar). *Geochimica Et*
766 *Cosmochimica Acta* 131, 196-212.

767 Mei, Y., Sherman, D.M., Liu, W., Etschmann, B., Testemale, D. and Brugger, J. (2015a) Zinc
768 complexation in chloride-rich hydrothermal fluids (25–600 °C): A thermodynamic model
769 derived from ab initio molecular dynamics. *Geochimica et Cosmochimica Acta* 150, 265-
770 284.

771 Mei, Y., Etschmann, B., Liu, W., Sherman, D.M., Barnes, S.J., Fiorentini, M.L., Seward, T.M.,
772 Testemale, D. and Brugger, J. (2015b) Palladium complexation in chloride- and bisulfide-
773 rich fluids: Insights from ab initio molecular dynamics simulations and X-ray absorption
774 spectroscopy. *Geochimica et Cosmochimica Acta* 161, 128-145.

775 Mei, Y., Etschmann, B., Liu, W., Sherman, D.M., Testemale, D. and Brugger, J. (2016)
776 Speciation and thermodynamic properties of zinc in sulfur-rich hydrothermal fluids:
777 Insights from ab initio molecular dynamics simulations and X-ray absorption spectroscopy.
778 *Geochimica et Cosmochimica Acta* 179, 32-52.

779 Mei, Y., Liu, W., Brugger, J., Sherman, D.M. and Gale, J.D. (2018) The dissociation
780 mechanism and thermodynamic properties of HCl(aq) in hydrothermal fluids (to 700 °C,
781 60 kbar) by ab initio molecular dynamics simulations. *Geochimica et Cosmochimica Acta*
782 226, 84-106.

783 Mei, Y., Liu, W., Brugger, J. and Guan, Q. (2020) Gold solubility in alkaline and ammonia-
784 rich hydrothermal fluids: Insights from ab initio molecular dynamics simulations.
785 *Geochimica et Cosmochimica Acta* 291, 62-78.

786 Migdisov, A.A., Reukov, V.V. and Williams-Jones, A.E. (2006) A spectrophotometric study
787 of neodymium(III) complexation in sulfate solutions at elevated temperatures. *Geochimica*
788 *et Cosmochimica Acta* 70, 983-992.

789 Migdisov, A.A. and Williams-Jones, A.E. (2008) A spectrophotometric study of Nd(III),
790 Sm(III) and Er(III) complexation in sulfate-bearing solutions at elevated temperatures.
791 *Geochimica et Cosmochimica Acta* 72, 5291-5303.

792 Migdisov, A.A. and Williams-Jones, A. (2014) Hydrothermal transport and deposition of the
793 rare earth elements by fluorine-bearing aqueous liquids. *Mineralium Deposita* 49, 987-997.

794 Migdisov, A., Williams-Jones, A.E., Brugger, J. and Caporuscio, F.A. (2016) Hydrothermal
795 transport, deposition, and fractionation of the REE: Experimental data and thermodynamic
796 calculations. *Chemical Geology* 439, 13-42.

797 Migdisov, A., Guo, X., Nisbet, H., Xu, H. and Williams-Jones, A.E. (2019) Fractionation of
798 REE, U, and Th in natural ore-forming hydrothermal systems: Thermodynamic modeling.
799 *The Journal of Chemical Thermodynamics* 128, 305-319.

800 Miron, G.D., Leal, A.M.M. and Yapparova, A. (2019) Thermodynamic Properties of Aqueous
801 Species Calculated Using the HKF Model: How Do Different Thermodynamic and
802 Electrostatic Models for Solvent Water Affect Calculated Aqueous Properties? *Geofluids*
803 2019, 1-24.

804 Naumov, A. V. (2008). Review of the world market of rare-earth metals. *Russian Journal of*
805 *Non-Ferrous Metals*, 49(1), 14-22.

806 Navrotsky, A., Lee, W., Mielewczyk-Gryn, A., Ushakov, S.V., Anderko, A., Wu, H. and
807 Riman, R.E. (2015) Thermodynamics of solid phases containing rare earth oxides. *The*
808 *Journal of Chemical Thermodynamics* 88, 126-141.

809 Nazari-Dehkordi, T., Spandler, C., Oliver, N.H. and Wilson, R. (2020) Age, geological setting,
810 and paragenesis of heavy rare earth element mineralization of the Tanami region, Western
811 Australia. *Mineralium Deposita* 55, 107-130.

812 Oelkers, E.H. and Helgeson, H.C. (1990) Triple-ion anions and polynuclear complexing in
813 supercritical electrolyte solutions. *Geochimica et Cosmochimica Acta* 54, 727-738.

814 Ohta, A., Kagi, H., Tsuno, H., Nomura, M. and Kawabe, I. (2008) Influence of multi-electron
815 excitation on EXAFS spectroscopy of trivalent rare-earth ions and elucidation of change
816 in hydration number through the series. *American Mineralogist* 93, 1384-1392.

817 Panina, L. (2005) Multiphase carbonate-salt immiscibility in carbonatite melts: data on melt
818 inclusions from the Krestovskiy massif minerals (Polar Siberia). *Contributions to
819 Mineralogy and Petrology* 150, 19-36.

820 Patel, N., Dubins, D.N., Pomes, R. and Chalikian, T.V. (2011) Parsing partial molar volumes
821 of small molecules: A molecular dynamics study. *The Journal of Physical Chemistry B*
822 115, 4856-4862.

823 Proux, O., Biquard, X., Lahera, E., Menthonnex, J.-J., Prat, A., Ulrich, O., Soldo, Y., Trévisson,
824 P., Kapoujyan, G. and Perroux, G. (2005) FAME: A new beamline for X-ray absorption
825 investigations of very-diluted systems of environmental, material and biological interests.
826 *Physica Scripta* 2005, 970.

827 Ram, R., Becker, M., Brugger, J., Etschmann, B., Burcher-Jones, C., Howard, D., Kooyman,
828 P.J. and Petersen, J. (2019) Characterisation of a rare earth element-and zirconium-bearing
829 ion-adsorption clay deposit in Madagascar. *Chemical Geology* 522, 93-107.

830 Ravel, B. and Newville, M. (2005) ATHENA, ARTEMIS, HEPHAESTUS: data analysis for
831 X-ray absorption spectroscopy using IFEFFIT. *Journal of synchrotron radiation* 12, 537-
832 541.

833 Rehr, J.J., Kas, J.J., Prange, M.P., Sorini, A.P., Takimoto, Y. and Vila, F. (2009) Ab initio
834 theory and calculations of X-ray spectra. *Comptes Rendus Physique* 10, 548-559.

835 Richens, D.T. (2005) Ligand substitution reactions at inorganic centers. *Chemical reviews* 105,
836 1961-2002.

837 Richter, L., Diamond, L.W., Atanasova, P., Banks, D.A. and Gutzmer, J. (2018) Hydrothermal
838 formation of heavy rare earth element (HREE)–xenotime deposits at 100° C in a
839 sedimentary basin. *Geology* 46, 263-266.

840 Rielli, A., Tomkins, A.G., Nebel, O., Brugger, J., Etschmann, B., Zhong, R., Yaxley, G.M. and
841 Paterson, D. (2017) Evidence of sub-arc mantle oxidation by sulphur and carbon.
842 *Geochemical Perspectives Letters* 3, 124-132.

843 Rodinger, T., Howell, P.L. and Pomès, R. (2005) Absolute free energy calculations by
844 thermodynamic integration in four spatial dimensions. *The Journal of chemical physics*
845 123, 034104.

846 Roy, M., Gurman, S. and Van Dorssen, G. (1997) The amplitude reduction factor in EXAFS.
847 *Le Journal de Physique IV* 7, C2-151-C152-152.

848 Schijf, J. and Byrne, R.H. (2004) Determination of $\text{SO}_4\beta_1$ for yttrium and the rare earth
849 elements at $I = 0.66 \text{ m}$ and $t = 25^\circ\text{C}$ —implications for YREE solution speciation in sulfate-
850 rich waters. *Geochimica et Cosmochimica Acta* 68, 2825-2837.

851 Schijf, J. and Byrne, R.H. (2021) Speciation of yttrium and the rare earth elements in seawater:
852 Review of a 20-year analytical journey. *Chemical Geology* 584, 120479 (23 pp).

853 Shock, E. L., & Helgeson, H. C. (1988). Calculation of the thermodynamic properties and
854 transport properties of aqueous species and equation of state predictions to 5 kb and 1000
855 C. *Geochimica et Cosmochimica Acta*, 52(2009), 2036.

856 Shock, E. L., Sassani, D. C., Willis, M., & Sverjensky, D. A. (1997). Inorganic species in
857 geologic fluids: correlations among standard molal thermodynamic properties of aqueous
858 ions and hydroxide complexes. *Geochimica et Cosmochimica Acta*, 61(5), 907-950.

859 Smith, M.P., Henderson, P. and Campbell, L.S. (2000) Fractionation of the REE during
860 hydrothermal processes: constraints from the Bayan Obo Fe-REE-Nb deposit, Inner
861 Mongolia, China. *Geochimica et Cosmochimica Acta* 64, 3141-3160.

862 Spahiu, K., & Bruno, J. (1995). A selected thermodynamic database for REE to be used in
863 HLNW performance assessment exercises (No. SKB-TR--95-35). Swedish Nuclear Fuel
864 and Waste Management Co.

865 Sprik, M. (1998) Coordination numbers as reaction coordinates in constrained molecular
866 dynamics. *Faraday Discussions* 110, 437-445.

867 Sprik, M., Hutter, J. and Parrinello, M. (1996) Ab initio molecular dynamics simulation of
868 liquid water: Comparison of three gradient-corrected density functionals. *The Journal of*
869 *chemical physics* 105, 1142-1152.

870 Stefanski, J. and Jahn, S. (2020) Yttrium speciation in subduction-zone fluids from ab initio
871 molecular dynamics simulations. *Solid Earth* 11, 767-789.

872 Sverjensky, D., Shock, E. and Helgeson, H. (1997) Prediction of the thermodynamic properties
873 of aqueous metal complexes to 1000 °C and 5 kb. *Geochimica et Cosmochimica Acta* 61,
874 1359-1412.

875 Sverjensky, D.A., Harrison, B. and Azzolini, D. (2014) Water in the deep Earth: The dielectric
876 constant and the solubilities of quartz and corundum to 60kb and 1200°C. *Geochimica et*
877 *Cosmochimica Acta* 129, 125-145.

878 Testemale, D., Argoud, R., Geaymond, O. and Hazemann, J.-L. (2005) High pressure/high
879 temperature cell for x-ray absorption and scattering techniques. *Review of Scientific*
880 *Instruments* 76, 043905.

881 Tooth, B., Etschmann, B., Pokrovski, G.S., Testemale, D., Hazemann, J.-L., Grundler, P.V.
882 and Brugger, J. (2013) Bismuth speciation in hydrothermal fluids: An X-ray absorption
883 spectroscopy and solubility study. *Geochimica et Cosmochimica Acta* 101, 156-172.

884 Troullier, N. and Martins, J.L. (1991) Efficient pseudopotentials for plane-wave calculations.
885 *Physical Review B* 43, 1993-2006.

886 Vallet, V. and Grenthe, I. (2007) On the structure and relative stability of uranyl(VI) sulfate
887 complexes in solution. *Comptes Rendus Chimie* 10, 905-915.

888 VandeVondele, J. and Hutter, J. (2007) Gaussian basis sets for accurate calculations on
889 molecular systems in gas and condensed phases. *The Journal of Chemical Physics* 127,
890 114105.

891 Williams-Jones, A.E., Migdisov, A.A. and Samson, I.M. (2012) Hydrothermal mobilisation of
892 the rare earth elements—a tale of “ceria” and “yttria”. *Elements* 8, 355-360.

893 Williams-Jones, A. E., Samson, I. M., & Olivo, G. R. (2000). The genesis of hydrothermal
894 fluorite-REE deposits in the Gallinas Mountains, New Mexico. *Economic Geology*, 95(2),
895 327-341.

896 Wang, X., Wan, Y., and Chou, I. M. (2020). Fate of sulfate in seafloor hydrothermal systems:
897 Insights from in situ observation of the liquid–liquid phase separation in hydrothermal
898 fluids. *Solid Earth Sciences*, 6(1), 1-11.

899 Wood, S.A. (1990) The aqueous geochemistry of the rare-earth elements and yttrium: 2.
900 Theoretical predictions of speciation in hydrothermal solutions to 350 C at saturation water
901 vapor pressure. *Chemical Geology* 88, 99-125.

902 Wood, S.A. and Williams-Jones, A.E. (1994) The aqueous geochemistry of the rare-earth
903 elements and yttrium 4. Monazite solubility and REE mobility in exhalative massive
904 sulfide-depositing environments. *Chemical Geology* 115, 47-60.

905 Xie, Y., Li, Y., Hou, Z., Cooke, D.R., Danyushevsky, L., Dominy, S.C. and Yin, S. (2015) A
906 model for carbonatite hosted REE mineralisation — the Mianning–Dechang REE belt,
907 Western Sichuan Province, China. *Ore Geology Reviews* 70, 595-612.

908 Xing, Y., Etschmann, B., Liu, W., Mei, Y., Shvarov, Y., Testemale, D., Tomkins, A. and
909 Brugger, J. (2019) The role of fluorine in hydrothermal mobilization and transportation of
910 Fe, U and REE and the formation of IOCG deposits. *Chemical Geology* 504, 158-176.

911 Yardley, B.W. (2005) 100th Anniversary Special Paper: metal concentrations in crustal fluids
912 and their relationship to ore formation. *Economic Geology* 100, 613-632.

913 Zhang, W., & Yan, T. (2022). A molecular dynamics investigation of La³⁺ and Lu³⁺-ligand
914 speciation in aqueous solution. *Journal of Molecular Liquids*, 118367, 12 pp.

915

916